PARAMETRIC INSTABILITIES OF ROTOR-SUPPORT SYSTEMS WITH APPLICATION TO INDUSTRIAL VENTILATORS

Zdzisław Parszewski, Janusz Krodkiewski,
and Krzysztof Marynowski
Politechnika Łodzka
Łodz, Poland 90245

SUMMARY

Rotor-support systems interaction with parametric excitation is considered for both unequal principal shaft stiffnesses (generators) and off-set disc rotors (ventilators). Instability regions and types of instability are computed in the first case, and parametric resonances in the second case. Computed and experimental results are compared for laboratory machine models. A field case study of parametric vibrations in industrial ventilators is reported. Computed parametric resonances are confirmed in field measurements, and some industrial failures are explained. Also the dynamic influence and gyroscopic effect of supporting structures are shown and computed.

INTRODUCTION

With growing rotor speeds or machine capacities the influence of supporting structures on stability and critical speeds is of increasing importance, specially when some rotor parameters are variable. This is often the case in machines used in mining and power generating industries, for example, large generators, industrial ventilators, and turbopumps. The unequal rotor principal stiffnesses in the first instance and unequal principal moments of inertia of the ventilator disc in the second instance, with the flexible anisotropic support interaction, cause the parametric effect.

A 120-MW generator of Dolmel-Wrocław production is shown in figure 1. Its rotor is of 9.157 m length, with a span of 6.858 m between bearings. The wiring slots distribution gives rise to small unequality of the rotor principal stiffnesses k_x, k_y. Two types of mine ventilators are shown in figure 2: large ventilator No. I of the type SLM (fig. 2(a)) of nominal output of 320 m/min, and universal ventilator No. II of type FKD-30 (fig. 2(b)). The first has an overhang shaft of full length 0.908 m. The disc is between bearings in the second ventilator with a shaft of 0.773 m length. Production errors cause the unequality of principal moments of inertia of the disc.

GENERAL THEORY

The rotor-support system can be considered as two connected and dynamically interacting subsystems. One (rotor) is a discrete parametric system (fig. 3, bold lines). The second is nonparametric, contains the whole supporting structure, and is usually very complicated. A receptance (impedance) matrix is hence used for description of its dynamic behavior. Its elements can then be measured if not calculated. All (usually infinity) but the connecting coordinates

of the supporting structure can be eliminated (ref. 6) from the equations of
motion of the systems, giving their general matrix form

$$\underset{\mathcal{H}\times\mathcal{H}}{\mathbf{M}(t)}\ddot{\mathbf{x}} + \left[\underset{\mathcal{H}\times\mathcal{H}}{\mathbf{C}(t)} + \frac{1}{\beta}\underset{\mathcal{H}\times\mathcal{H}}{\boldsymbol{\gamma}_u(\beta)}\right]\dot{\mathbf{x}} + \left[\underset{\mathcal{H}\times\mathcal{H}}{\mathbf{K}(t)} + \underset{\mathcal{H}\times\mathcal{H}}{\boldsymbol{\gamma}_r(\beta)}\right]\underset{\mathcal{H}}{\mathbf{x}} = \underset{\mathcal{H}}{\mathbf{G}} + \underset{\mathcal{H}}{\mathbf{P}}\sin\omega t + \underset{\mathcal{H}}{\mathbf{Q}}\cos\omega t \qquad (1)$$

Here all the matrices are of the order equal to the sum of the number of de-
grees of freedom of the parametric subsystem (rotor) and the number of connect-
ing coordinates. In the cases considered, for instance, the last number is
four (fig. 2); γ_r and γ_u are, respectively, real and imaginary parts of the
dynamic impedances of the supporting structure along the connecting coordinates;
G, P, and Q are force vectors. For an offset disc mounted flexibly (fig. 4)
or for a rotor of different principal stiffnesses (the two cases are here con-
nected only formally), the equations are

For a rotor of different principal stiffnesses

$$\mathbf{M}(t) = \mathbf{M}; \quad \mathbf{C}(t) = \mathbf{C}; \quad \mathbf{K}(t) = \mathbf{K} + \varepsilon(\mathbf{E}\cos\vartheta t + \mathbf{F}\sin\vartheta t) \qquad (2a)$$

For an offset disc and circular shaft

$$\mathbf{M}(t) = \mathbf{M} + \mathbf{d}(t); \quad \mathbf{C}(t) = \mathbf{C} + \mathbf{Z} + \mathbf{c}(t); \quad \mathbf{K}(t) = \mathbf{K} + \mathbf{d}(t) \qquad (2b)$$

where

$$\mathbf{M} = \begin{bmatrix} m & -S_{\xi\eta} & 0 & 0 & 0 \\ -S_{\xi\eta} & -B-B_{\xi\eta} & 0 & 0 & 0 \\ 0 & 0 & -m & S_{\xi\eta} & 0 \\ 0 & 0 & S_{\xi\eta} & -B-B_{\xi\eta} & 0 \\ 0 & 0 & 0 & 0 & -m \end{bmatrix} \quad \mathbf{Z} = \begin{bmatrix} 0 & 0 & 0 & 0 & 0 \\ 0 & 0 & 0 & 2\omega B & 0 \\ 0 & 0 & 0 & 0 & 0 \\ 0 & -2\omega B & 0 & 0 & 0 \\ 0 & 0 & 0 & 0 & 0 \end{bmatrix} \quad \boldsymbol{\gamma}_r = \begin{bmatrix} \gamma_{x\beta_x} & \gamma_{x\mu_y} & 0 & 0 & 0 \\ \gamma_{\psi_y\beta_x} & \gamma_{\psi_y\mu_y} & 0 & 0 & 0 \\ 0 & 0 & \gamma_{\psi_y\beta_y} & \gamma_{\psi\mu_x} & 0 \\ 0 & 0 & \gamma_{\psi_x\beta_y} & \gamma_{\psi_x\mu_x} & 0 \\ 0 & 0 & 0 & 0 & \gamma_{z\beta_z} \end{bmatrix}$$

$$(3)$$

$$\mathbf{b} = \begin{bmatrix} 0 & 0 & & 0 & 0 & & 0 \\ 0 & -\Delta B\cos2\omega t + D_\zeta\sin2\omega t & 0 & \Delta B\sin2\omega t + D_\zeta\cos2\omega t & S_{\eta\zeta}\cos\omega t - S_{\zeta\zeta}\sin\omega t \\ 0 & 0 & & 0 & 0 & & 0 \\ 0 & \Delta B\sin2\omega t + D_\zeta\cos2\omega t & 0 & \Delta B\cos2\omega t - D_\zeta\sin2\omega t & -S_{\eta\zeta}\sin\omega t - S_{\zeta\zeta}\cos\omega t \\ 0 & S_{\eta\zeta}\cos\omega t - S_{\zeta\zeta}\sin\omega t & 0 & -S_{\eta\zeta}\sin\omega t - S_{\zeta\zeta}\cos\omega t & 0 \end{bmatrix} \quad \mathbf{X} = \begin{bmatrix} x \\ \psi_y \\ y \\ \psi_x \\ z \end{bmatrix} \qquad (4)$$

$$\mathbf{C} = \begin{bmatrix} 0 & 0 & & 0 & 0 & & 0 \\ 0 & 2\Delta B\omega\sin2\omega t + 2D_\zeta\omega\cos2\omega t & 0 & 2\Delta B\omega\cos2\omega t - 2D_\zeta\omega\sin2\omega t & 0 \\ 0 & 0 & & 0 & 0 & & 0 \\ 0 & 2\Delta B\omega\sin2\omega t + 2D_\zeta\sin2\omega t & 0 & -2\Delta B\omega\sin2\omega t - 2D_\zeta\omega\cos2\omega t & 0 \\ 0 & -2\omega(S_{\eta\zeta}\sin\omega t + S_{\zeta\zeta}\cos\omega t) & 0 & -2\omega(S_{\eta\zeta}\cos\omega t - S_{\zeta\zeta}\sin\omega t) & 0 \end{bmatrix} \quad (5) \quad \mathbf{P} = \begin{bmatrix} -\omega^2 S_{\zeta\zeta} \\ -D_\zeta \\ \omega^2 S_{\eta\zeta} \\ -D\eta \\ \omega^2(\gamma_{\psi_y}S_{\zeta\zeta} + \gamma_{x\zeta}S_{\eta\zeta}) \end{bmatrix}$$

$$\mathbf{d} = \begin{bmatrix} 0 & 0 & & & 0 & 0 & & 0 \\ 0 & 0 & & & 0 & 0 & & 0 \\ 0 & 0 & & & 0 & 0 & & 0 \\ 0 & 0 & & & 0 & 0 & & 0 \\ 0 & -\omega^2(S_{\eta\varsigma}\cos\omega t - S_{\varsigma\varsigma}\sin\omega t) & 0 & \omega^2(S_{\eta\varsigma}\sin\omega t + S_{\varsigma\varsigma}\cos\omega t) & 0 \end{bmatrix} \quad (6)$$

$$(7) \quad \mathbf{Q} = \begin{bmatrix} \omega^2 S_{\eta\varsigma} \\ D_\eta \\ \omega^2 S_{\varsigma\varsigma} \\ -D_\varsigma \\ -\omega^2(\gamma_{y3}S_{\eta\varsigma} - \gamma_{x3}S_{\varsigma\varsigma}) \end{bmatrix}$$

where $S_{\xi\eta}, \dots B_{\eta\varsigma}$ are the first and second moments of the rotor mass with respect to the coordinate planes $\xi\eta\varsigma$ connected with the rotor; D_ξ, D_η, D_ς are corresponding deviation moments; and

$$B = \tfrac{1}{2}\left(B_{\eta\varsigma} + B_{\varsigma\varsigma}\right) \qquad \Delta B = \tfrac{1}{2}\left(B_{\eta\varsigma} - B_{\varsigma\varsigma}\right) \tag{8}$$

Finally

$$\beta_i^{(\pm)} = \frac{i\vartheta \pm 2\mu}{2} \tag{9}$$

where μ and θ are the arguments of the solutions

$$\mathbf{x} = e^{j\mu t} \sum_{i=0}^{\infty}\left(\mathbf{a}_i \sin \frac{i\vartheta}{2} t + \mathbf{b}_i \cos \frac{i\vartheta}{2} t\right) \tag{10}$$

of the homogenous part of equation (1) at stability limits.

Instability

The conditions of existence of steady solutions (10), giving the boundary equations in the stability region, in the equivalent forms for odd or even numerals i, are

$$\begin{vmatrix} g_{11} & & & & \cdots \\ & g_{32} & & & \cdots \\ & & \ddots & & \cdots \\ & & & g_{ii} & \cdots \\ \cdots & \cdots & \cdots & \cdots & \cdots \end{vmatrix} = 0 \tag{11}$$

Consecutive approximations are shown with broken lines in equation (11). The first approximation is

$$g_{11} = \begin{vmatrix} -(\beta_-)^2 M + K + \dot{\gamma}_T(\beta_-) & -\frac{1}{2}\varepsilon E & -\beta_- C + \dot{\gamma}_u(\beta_-) & \frac{1}{2}\varepsilon F \\[4pt] -\frac{1}{2}\varepsilon E & -(\beta_+)^2 M + K + \dot{\gamma}_T(\beta_+) & \frac{1}{2}\varepsilon F & -\beta_+ C + \dot{\gamma}_u(\beta_+) \\[4pt] \beta_+ C + \dot{\gamma}_u(\beta_-) & \frac{1}{2}\varepsilon F & -(\beta_-)^2 M + K + \dot{\gamma}_T(\beta_-) & \frac{1}{2}\varepsilon E \\[4pt] \frac{1}{2}\varepsilon F & \beta_+ C + \dot{\gamma}_u(\beta_+) & \frac{1}{2}\varepsilon E & -(\beta_+)^2 M + K + \dot{\gamma}_T(\beta_+) \end{vmatrix} = O \qquad (12)$$

The instabilities occur in the vicinity of circular frequencies

$$\theta_{jk} = \frac{\lambda_j + \lambda_k}{n} \qquad n = 1, 2, 3, \ldots \qquad (13)$$

The width of the instability region depends on ε and damping C. Here λ_j are the natural frequencies of the system, being the roots of equation (12) at zero parametric excitation ($\varepsilon = 0$) and no damping ($C = 0$, $\gamma_u = 0$).

Resonance Speeds

Forced vibrations analysis gives for the resonance speeds ω_{cr} (refs. 3 and 6)

$$\left. \begin{aligned} (2n - 1)\omega_{cr} &= \lambda_i(\omega_{cr}) \\[8pt] 2n\,\omega_{cr} &= \lambda_z(\omega_{cr}) \end{aligned} \right\} \qquad (14)$$

and

Here λ_z is the axial natural circular frequency of the system.

LABORATORY MODEL TESTS AND COMPUTATIONS

Computations were done for a laboratory model (fig. 5) and compared with the tests results.

Generator Model – Instabilities

The instability regions were computed for the model with the shaft of different principal stiffnesses k_x, k_y and rotor block between bearing (no disc 5 in fig. 5). The determinants (12) give equations of instability region boundaries in the form $|W(\mu,\theta)| = 0$. Their roots μ_i, θ_i define the stability limits. An example of computed results is given in figure 6. This diagram corresponds to the second-order combined instability region $0.5(\theta_{x1} + \theta_{y1})$ around point N (fig. 6). The solutions of the equation

$$|W(\mu,\theta)| = 0$$

for zero parametric excitation ($\varepsilon = 0$) and no damping ($C = 0$, $\gamma_u = 0$) are straight lines

$$\beta^{(\pm)} = \frac{i\theta \pm 2\mu}{2} = \lambda_j$$

intersecting at point N (fig. 6). For finite parametric excitation the lines curve and do not intersect, separating in the direction θ for frequencies sums $1/n(\lambda_j + \lambda_k)$ or in the direction μ for their differences $1/n(\lambda_j - \lambda_k)$. Hence there are no instabilities (also with no damping) corresponding to the frequency differences. The curves in figure 6 correspond to constant values of the determinant, and its zero values (denoted with the crosses) give the instability region. They approach each other with increasing damping and, over its limiting value, instability disappears. This was traced with changing shaft length ΔL, and computed and experimental results are compared in figure 7. Corresponding oscillograms for the x and y directions are given in figure 8. The instability region discussed here is denoted by 1 in the instability regions diagram (fig. 9). There are computed instability regions (with the type of instability) shown in figure 9 and against them the observed experimental instabilities shown with the crosses.

Ventilator Model - Resonance Speeds

Analysis of forced vibrations was done for the model with circular shaft and the disc 5 (fig. 5) slightly offset. Hence $B_{\eta\zeta}$ and $B_{\xi\zeta}$ are not equal and $S_{\eta\zeta}, \ldots, D_{\zeta}$ as well as disbalance forces P and Q are not zero, but $\varepsilon = 0$. Graphical solution of equation (1) for the laboratory model is given in figure 10. The continuous curved lines are the computed natural frequency curves. Abscissas of their points of intersection with the straight lines $\lambda = \omega$ (principal), $\lambda = 2\omega$, $\lambda = 3\omega \ldots$ give the parametric resonance speeds, with one, two, three, ... vibration cycles per one revolution. Computed values of 10 resonance speeds (taken from diagram, fig. 10) in s^{-1} are

$$\omega_{cr1} = 20, \quad \omega_{cr2} = 36, \quad \omega_{cr3} = 46, \quad \omega_{cr4} = 58, \quad \omega_{cr5} = 82,$$

$$\omega_{cr6} = 99, \quad \omega_{cr7} = 108, \quad \omega_{cr8} = 112, \quad \omega_{cr9} = 140, \quad \omega_{cr10} = 175$$

Experimental resonance diagrams measured for the right support (fig. 5) are given in figure 11 as continuous broken and dotted lines for the directions y, x, z, respectively. They compare well with the computed values from figure 10. The vibrations recorded for speeds close to resonance, numbered in the diagrams (figs. 10 and 11) are shown in figure 12. It can be seen that close to resonance speed of the type $n\omega_{cr} = \lambda_i(\omega_{cr})$ vibrations of frequency $n\omega$ dominate. Comparison of figures 10, 11, and 12 shows good consistency of theoretical and experimental results.

FIELD CASE STUDY

The above results were applied in field studies of vibrations of industrial ventilators that developed repeated failures (shaft breakages). These were ventilators No. II of the type FKD-30 (fig. 2(b)) mentioned in the INTRODUCTION.

Analysis

The model of the ventilator consists of two subsystems: the discretized rotor (fig. 13) described in table 1 and the supporting structure containing the ventilator body with bearings and foundation (fig. 14). The supporting structure, for its dynamic interaction with the rotor, was dynamically defined with its receptance matrix along the connecting coordinates x_1, y_1, x_2, y_2

$$\begin{bmatrix} c_{x1x1} & c_{x1x2} & c_{x1y1} & c_{x1y2} \\ c_{x2x1} & c_{x2x2} & c_{x2y1} & c_{x2y2} \\ c_{y1x1} & c_{y1x2} & c_{y1y1} & c_{y1y2} \\ c_{y2x1} & c_{y2x2} & c_{y2y1} & c_{y2y2} \end{bmatrix} = [c_{ik}] \tag{15}$$

The receptances c_{ik} were measured on site. The measuring scheme is given in figure 15. The notations in figure 15 are 1 - ventilator type II, 2 - electro-dynamic exciter, 3 - displacement pickup, 4 - generator, 5 - vibration measuring apparatus, 6 - two-ray cathode oscilloscope, 7 - frequency meter, 8 - phase meter, 9 - ammeter.

The exciting force was measured indirectly (by current measurement). Receptance diagrams are given in figure 16. Because of symmetry all the cross receptances for the perpendicular directions are zero. The other equal pairs are denoted c_{iix}, c_{iiy}, c_{ijx}, c_{ijy}, where $i = 1, 2$. On the basis of the receptance matrix (15) the impedance (dynamic stiffness) matrix

$$[\gamma_{ik}] = [c_{ik}]^{-1}$$

was calculated and introduced in the computing program. Forced vibrations were found as partial solutions of equation (1) for the case of equal rotor stiffnesses by application of the small-parameter method. Their analysis gives the formulas (14) for the resonance speeds. Graphical solution is given in figure 17. The frequency lines are the solutions of the homogenous part of equation (1). With the approximation used, there are computed two principal resonance speeds (in s^{-1}), 344 and 280; two subharmonic ones of second order (of two cycles of vibration per revolution), 172 and 142; and two of third order, 114 and 94.

388

Experimental Measurement on Site

An experimental resonance test was made on site (in the mine) in the ventilator II in working condition. The measuring arrangement is shown in figure 18. Here 1 denotes the ventilator tested; 2 denotes the dc motor; 3 denotes the transformer displacement transducer; 4 denotes the vibration measuring apparatus; 5 the cathode ray oscilloscope; and 6 the frequency meter.

The resonance diagram for the supports for the practically allowed speed range from approximately 1200 to 2100 rpm is given in figure 19. The two observed subharmonic resonances, 138 and 174 s^{-1}, are in this speed range; both of second order are very close to the corresponding computed values, 142 and 172 s^{-1}.

CONCLUSIONS

The second-order subharmonic of frequency 142 s^{-1} coincided with the nominal working speed of ventilator II, which was below 1500 rpm. Hence it was the second-order parametric resonance that was responsible for the shaft breakages. Supporting structure appreciably lowers critical speeds. The gyroscopic effect was also considered and computed. It is specially visible in the ventilators with the overhang rotor. The frequency diagram for that type of ventilator, designated No. I in the INTRODUCTION, is given in figure 20. Important gyroscopic-effect influence is visible. It was the principal resonance at 144 s^{-1} that was responsible for the failures in those ventilators with nominal working speed below 1500 rpm.

REFERENCES

1. Bolotin, W. W.: Dinamiczeskaja ustoicivost uprugich sistem. GIT-TL, Moskva, 1956.

2. Szemplińska-Stupnicka, W.: Przyblizone metody analityczne badania niestateczności parametrycznej. Ossolineum, PAN, Warszawa, 1976.

3. Parszewski, Z.; Krodkiewski, J.: Stability and Critical Speeds of Non-Circular Shafts on Flexible Anisotropic Supports. Archiwum Budowy Maszyn No. 2, 1975.

4. Krodkiewski, J.: Proc. V. World Congress TMM, Montreal, 1979.

5. Krodkiewski, J.: Habilitation thesis, Politechnika Łódzka, Lódź, 1980.

6. Krodkiewski, J.; Marynowski, K.; Parszewski, Z.: Instabilities of Parametric Rotor-Support Systems. Proc. Conf. Vibrations in Rotating Machinery, Cambridge, 1980, I. Mech. Eng.
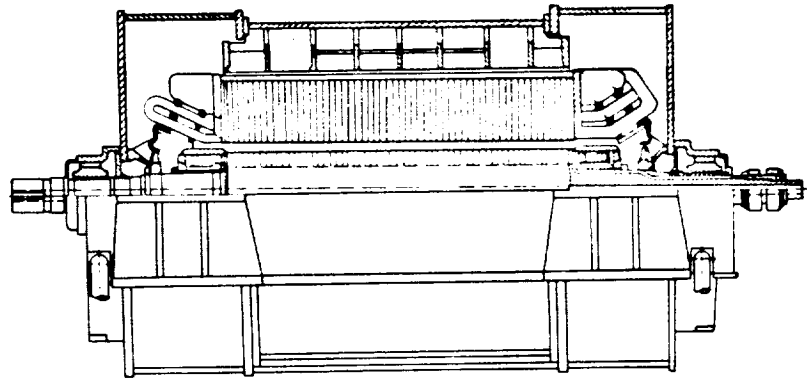
Fig.1
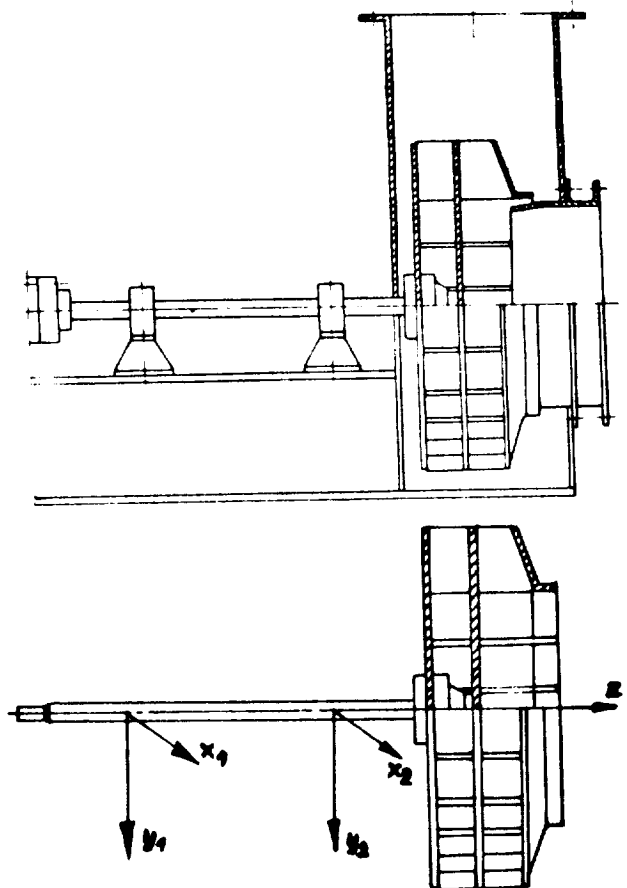
Fig.2a
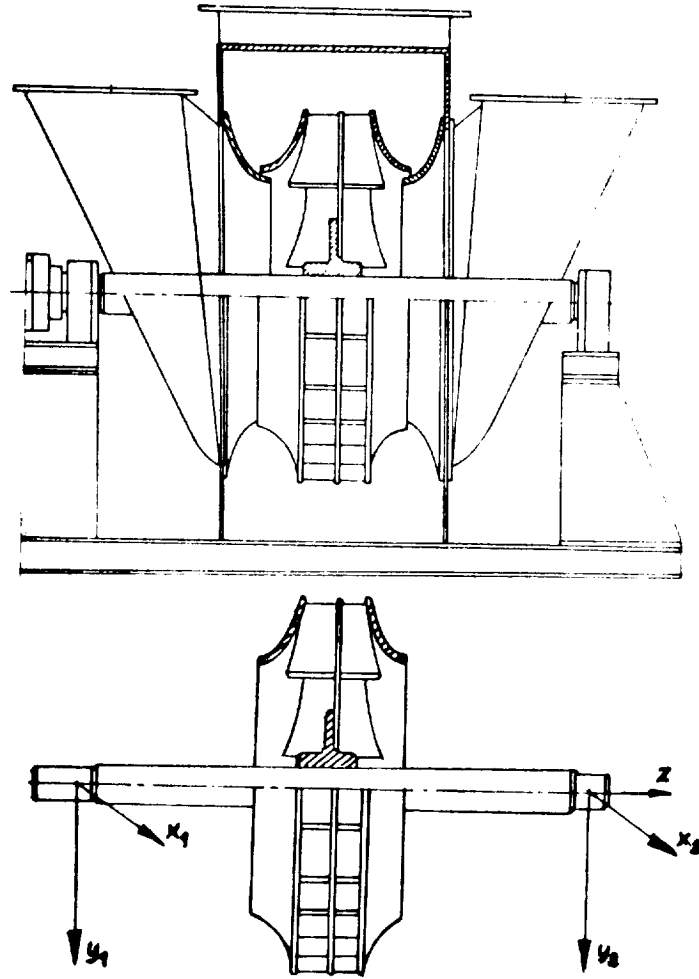
Fig.2b
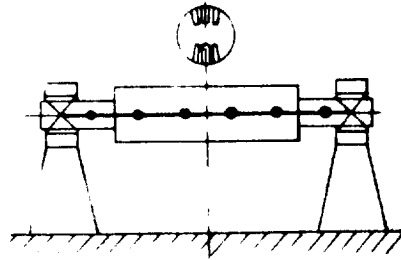
Fig.3a
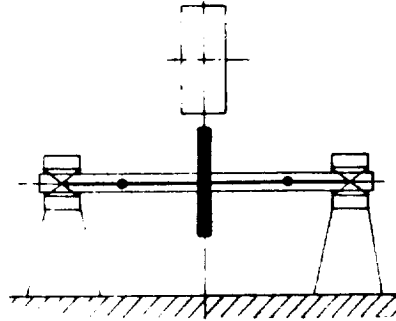
Fig.3b
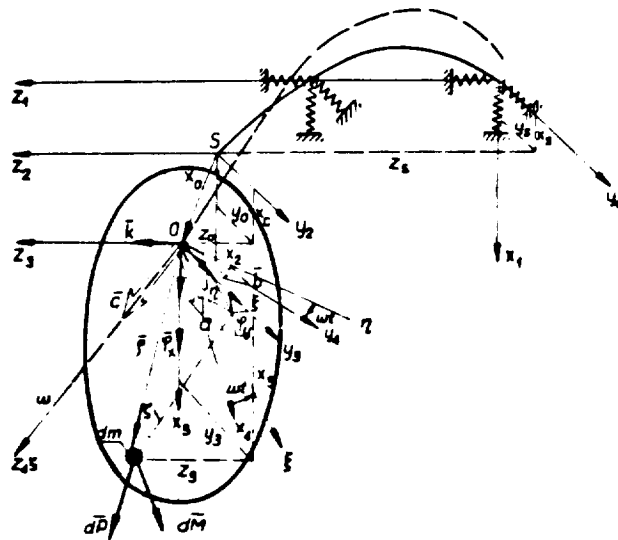
Fig.4
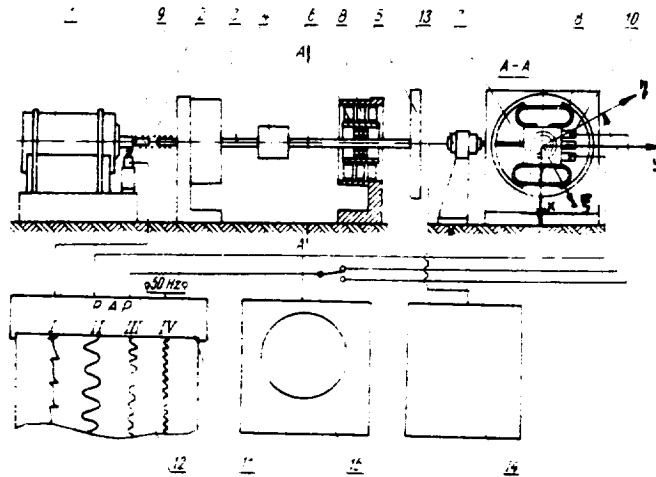
Fig.5 Scheme of model stand
1-DC motor,2-elastic coupling,
3-shaft,4-rotor mass,5-disc,6-ball
bearing,7-anisotropic bearing,
8-flat springs,9-inductive sensor,
10-piezo-electric sensors,11-re-
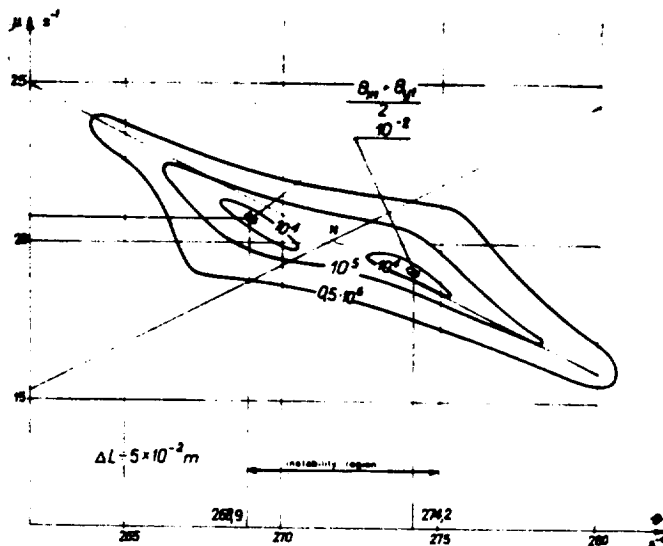corder,12-recorder tape,13-ele-
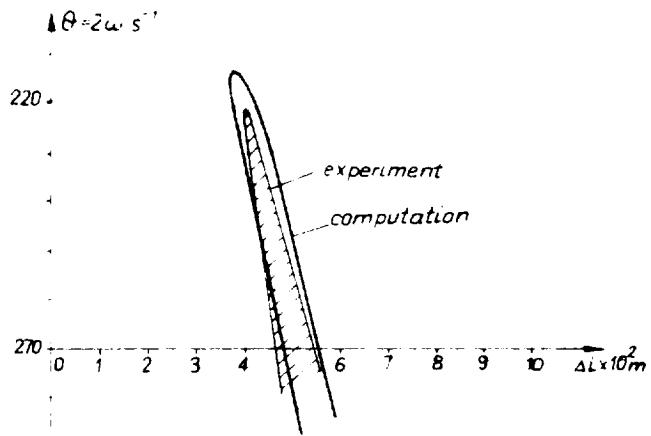ctrodynamic exciter,14-generator
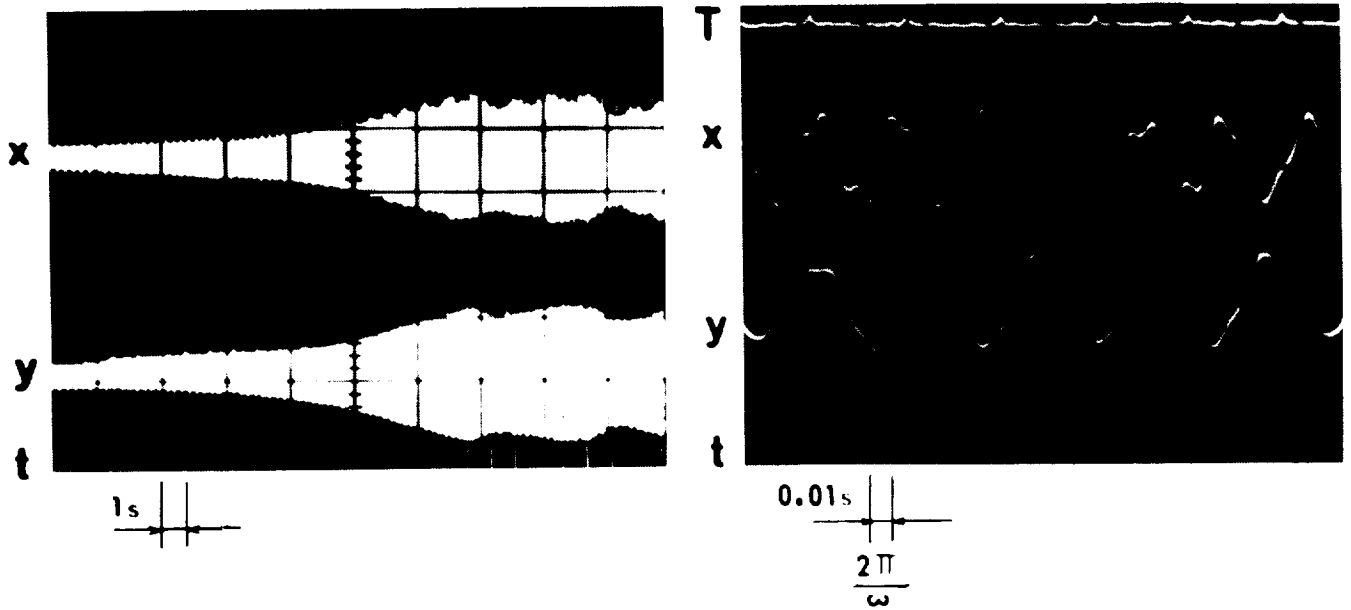of harmonic vibration,15-cathode
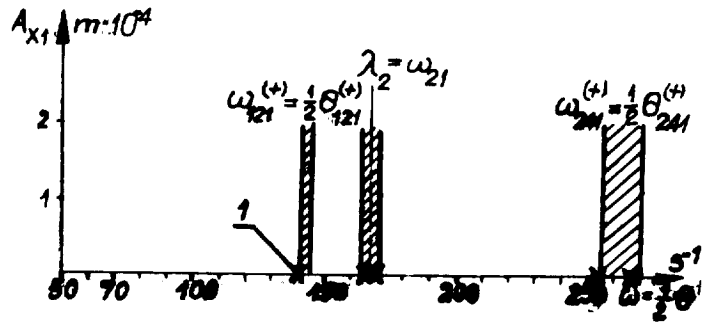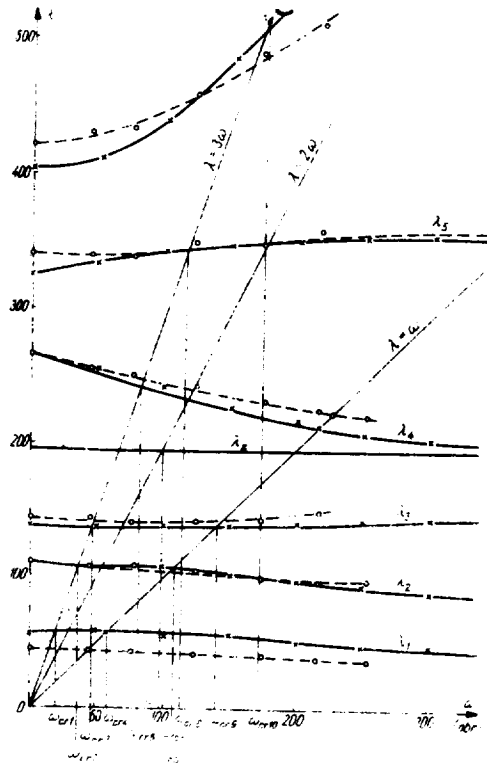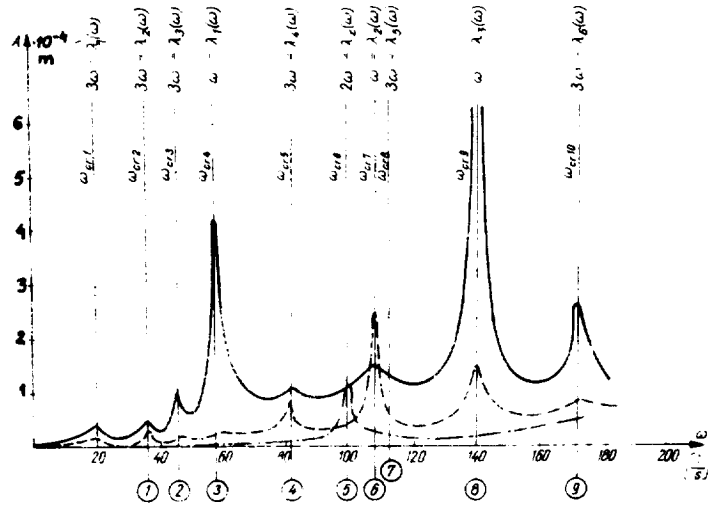oscilloscope.

Fig.6

Fig. 7

Fig. 8

Fig. 9

Fig. 10

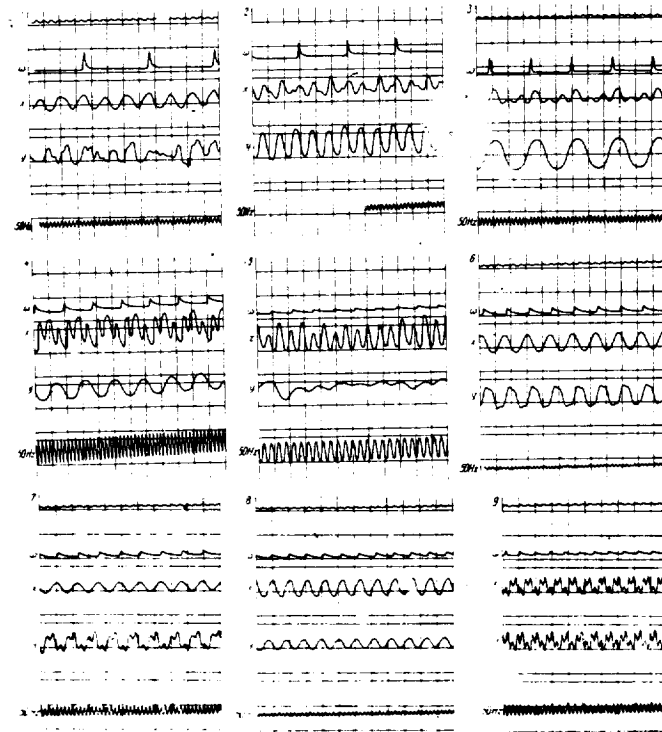Fig. 11 Resonance diagram of right
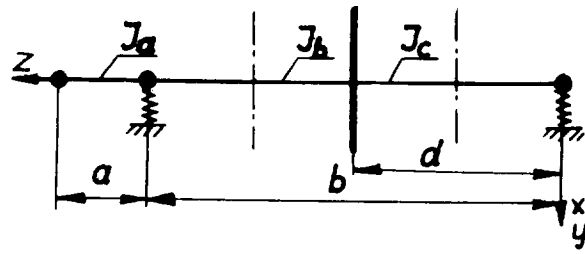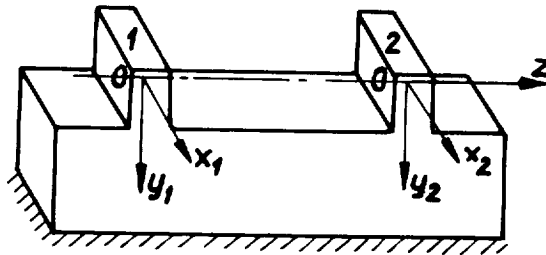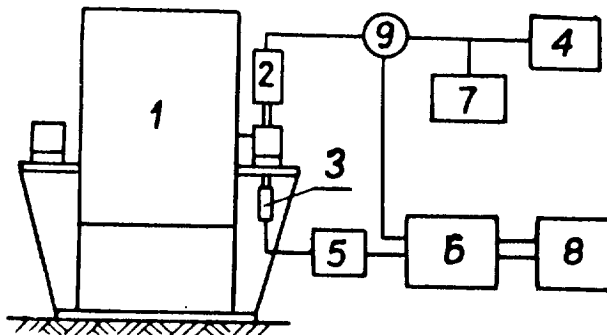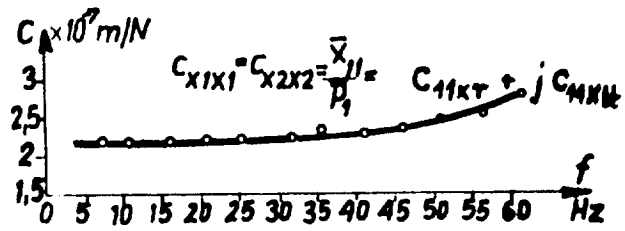support vibration of model stand.

Fig.12

396

Fig.13

Fig.14

Fig.15
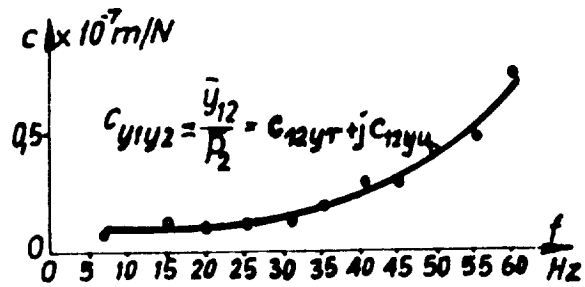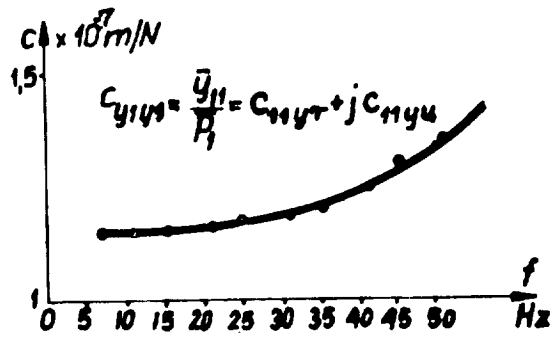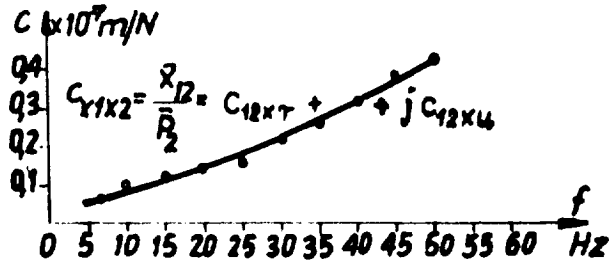
Fig.16
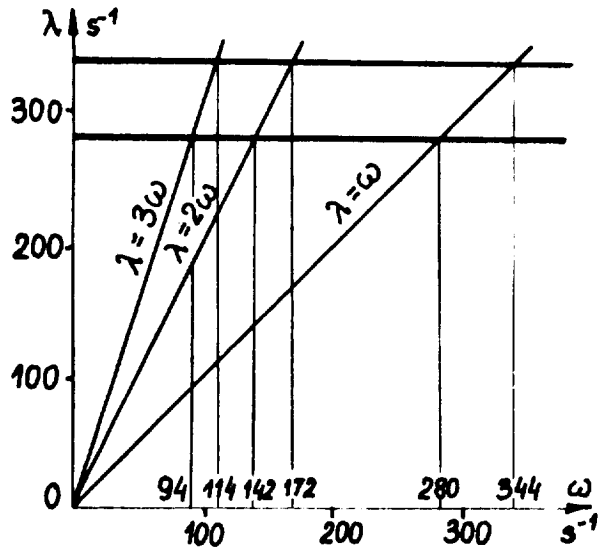
Fig.17
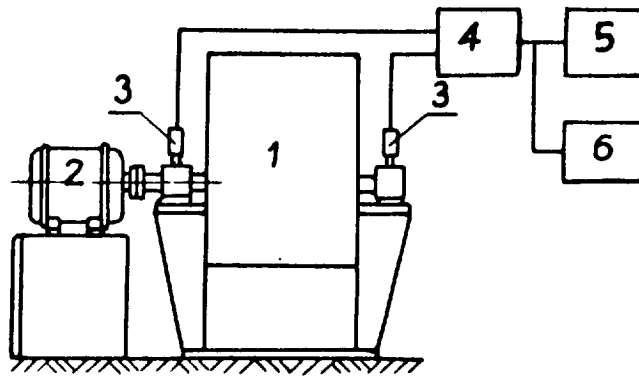
Fig.18
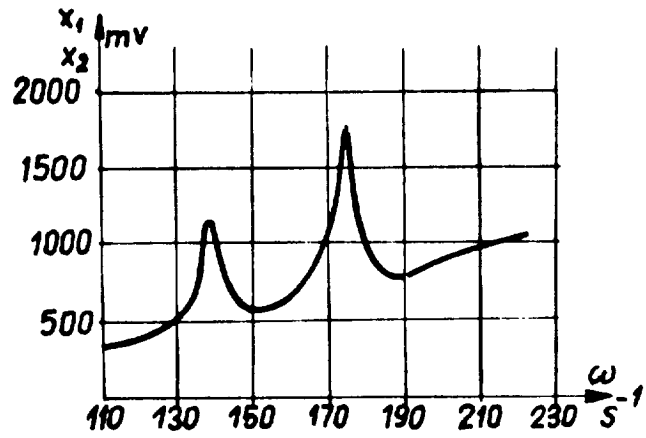
Fig.19
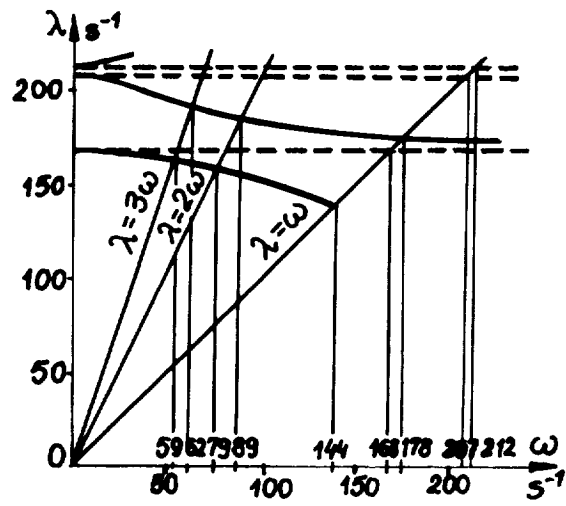
Fig.20

Tabl. 1

m_0	4,0221 kg	$B_{1,2}$	0,1995 kgm²	J_b	12,56·10⁻⁸ m⁴
m_1	2,3544 kg	$B_{0,2}$	0,3167 kgm²	J_c	10⁻⁸ m⁴
m_2	21,4839 kg	a	0,096 m	μ_0	0
m_3	0	b	0,677 m	μ_2	0,01 m
m_4	2,0601 kg	c	0	E	20,6·10¹⁰ Nm⁻²
B_1	0	d	0,3385 m		
$B_{0,1}$	0	J_a	6,55·10⁻⁸ m⁴		

400